parison between Fig. 3, A and D. The simulated B_s profile (Fig. 3D) also agrees reasonably well with the experimentally extracted B_s (Fig. 3A) given that there are some differences in shape and uncertainty in the exact boundary conditions. The main discrepancy is that the experimental B_s profile appears much more uniform than the simulated one, which may be attributed to spatial averaging of the LDOS over the magnetic length scale of ~1.5 nm. The simulated and experimental nanobubbles both exhibit a relatively uniform strain-induced pseudo–magnetic field of 200 to 400 T across the central region with increasing field at the edges.

The exceptional flexibility and strength of graphene membranes (*28*, *29*) coupled with the large strain-induced fields observed suggest that strain engineering of nanoscale energy levels (*11*, *30*) may be a viable means of controlling the electronic structure of graphene, even at room temperature. The experimental demonstration of these enormous pseudo–magnetic fields also provides a new basis for the study of extreme high magnetic field regimes in a condensed-matter environment.

References and Notes

1. A. H. Castro Neto, F. Guinea, N. M. R. Peres, K. S. Novoselov, A. K. Geim, *Rev. Mod. Phys.* **81**, 109 (2009).
2. A. K. Geim, K. S. Novoselov, *Nat. Mater.* **6**, 183 (2007).
3. P. R. Wallace, *Phys. Rev.* **71**, 622 (1947).
4. F. Guinea, M. I. Katsnelson, A. K. Geim, *Nat. Phys.* **6**, 30 (2010).
5. F. Guinea, A. K. Geim, M. I. Katsnelson, K. S. Novoselov, *Phys. Rev. B* **81**, 035408 (2010).
6. F. Guinea, M. I. Katsnelson, M. A. H. Vozmediano, *Phys. Rev. B* **77**, 075422 (2008).
7. Y. B. Zhang, Y. W. Tan, H. L. Stormer, P. Kim, *Nature* **438**, 201 (2005).
8. K. S. Novoselov *et al.*, *Nature* **438**, 197 (2005).
9. K. I. Bolotin, F. Ghahari, M. D. Shulman, H. L. Stormer, P. Kim, *Nature* **462**, 196 (2009).
10. X. Du, I. Skachko, F. Duerr, A. Luican, E. Y. Andrei, *Nature* **462**, 192 (2009).
11. V. M. Pereira, A. H. Castro Neto, *Phys. Rev. Lett.* **103**, 046801 (2009).
12. Materials and methods are available as supporting material on *Science* Online.
13. T. A. Land, T. Michely, R. J. Behm, J. C. Hemminger, G. Comsa, *Surf. Sci.* **264**, 261 (1992).
14. M. Enachescu, D. Schleef, D. F. Ogletree, M. Salmeron, *Phys. Rev. B* **60**, 16913 (1999).
15. A. B. Preobrajenski, M. L. Ng, A. S. Vinogradov, N. Martensson, *Phys. Rev. B* **78**, 073401 (2008).
16. M. Gao *et al.*, *Appl. Phys. Lett.* **96**, 053109 (2010).
17. P. Sutter, J. T. Sadowski, E. Sutter, *Phys. Rev. B* **80**, 245411 (2009).
18. J. A. Stroscio, W. J. Kaiser, *Scanning Tunneling Microscopy* (Academic Press, San Diego, CA, 1993).
19. J. Wiebe *et al.*, *Phys. Rev. B* **72**, 193406 (2005).
20. Y. B. Zhang *et al.*, *Nat. Phys.* **4**, 627 (2008).
21. V. W. Brar *et al.*, *Appl. Phys. Lett.* **91**, 122102 (2007).
22. G. M. Rutter *et al.*, *Science* **317**, 219 (2007).
23. V. W. Brar *et al.*, *Phys. Rev. Lett.* **104**, 036805 (2010).
24. J. Akola, H. P. Heiskanen, M. Manninen, *Phys. Rev. B* **77**, 193410 (2008).
25. D. L. Miller *et al.*, *Science* **324**, 924 (2009).
26. G. Li, E. Y. Andrei, *Nat. Phys.* **3**, 623 (2007).
27. H. S. Seung, D. R. Nelson, *Phys. Rev. A* **38**, 1005 (1988).
28. C. Lee, X. D. Wei, J. W. Kysar, J. Hone, *Science* **321**, 385 (2008).
29. J. S. Bunch *et al.*, *Nano Lett.* **8**, 2458 (2008).
30. W. Z. Bao *et al.*, *Nat. Nanotechnol.* **4**, 562 (2009).
31. Research supported by the Director, Office of Science, Office of Basic Energy Sciences, Materials Sciences and Engineering Division, of the U.S. Department of Energy (DOE) under contract no. DE-AC02-05CH11231 (instrumentation development and materials synthesis) and DOE contract no. DE-FG02-08ER46512 (experimental data analysis), by the Office of Naval Research Multidisciplinary University Research Initiative (MURI) award no. N00014-09-1-1066 (experimental STM measurements) and MURI award no. N00014-09-1-1063 (electronic structure calculations), and by Ministerio de Ciencia e Innovación (MICINN) (Spain), award nos. FIS2008-00124/CSD2007-00010 (continuum elasticity simulations). A.H.C.N. acknowledges the support of the Miller Institute for Basic Research. S.A.B. and K.L.M. acknowledge fellowship support from Natural Sciences and Engineering Research Council (Canada) and NSF, respectively. The authors declare no competing financial interests. Requests for materials should be addressed to M.F.C.

Supporting Online Material

www.sciencemag.org/cgi/content/full/329/5991/544/DC1
Materials and Methods
SOM Text
Figs. S1 to S7
References

30 April 2010; accepted 29 June 2010
10.1126/science.1191700

Probing the Superfluid–to–Mott Insulator Transition at the Single-Atom Level

W. S. Bakr,[1] A. Peng,[1] M. E. Tai,[1] R. Ma,[1] J. Simon,[1] J. I. Gillen,[1] S. Fölling,[1,2] L. Pollet,[1] M. Greiner[1]*

Quantum gases in optical lattices offer an opportunity to experimentally realize and explore condensed matter models in a clean, tunable system. We used single atom–single lattice site imaging to investigate the Bose-Hubbard model on a microscopic level. Our technique enables space- and time-resolved characterization of the number statistics across the superfluid–Mott insulator quantum phase transition. Site-resolved probing of fluctuations provides us with a sensitive local thermometer, allows us to identify microscopic heterostructures of low-entropy Mott domains, and enables us to measure local quantum dynamics, revealing surprisingly fast transition time scales. Our results may serve as a benchmark for theoretical studies of quantum dynamics, and may guide the engineering of low-entropy phases in a lattice.

Microscopic measurements can reveal properties of complex systems that are not accessible through statistical ensemble measurements. For example, scanning tunneling microscopy has allowed physicists to identify the importance of nanoscale spatial inhomogeneities in high-temperature superconductivity (*1*), and single-molecule microscopy (*2*) has enabled studies of local dynamics in chemical reactions, revealing the importance of multiple reaction pathways (*3*). Whereas previous ultracold quantum gas experiments focused primarily on statistical ensemble measurements, the recently introduced single atom–single lattice site imaging technique in a quantum gas microscope (*4*) opens the door for probing and controlling quantum gases on a microscopic level. Here, we present a microscopic study of an atom-lattice system that realizes the bosonic Hubbard model and exhibits a quantum phase transition from a superfluid to a Mott insulator (*5*–*7*).

In the weakly interacting superfluid regime, the many-body wave function factorizes into a product of states with well-defined phase on each lattice site, known as coherent states, with Poissonian number fluctuations. As the strength of the interaction increases, the number distribution is narrowed, resulting in a fixed atom number state on each site deep in the Mott insulator regime. We study this change in the number statistics across the transition; these microscopic studies are complementary to previous experiments that have focused on measuring ensemble properties such as long-range phase coherence, excitation spectra, or compressibility (*7*–*9*). Local properties such as on-site number statistics (*10*) had been accessible only indirectly (*8*, *11*, *12*) and were averaged over several shells of superfluid and Mott insulating domains in the inhomogeneous system, complicating quantitative interpretation. More recently, the shell structure was imaged through tomographic (*13*), spectroscopic (*14*), and in situ imaging techniques, coarse-grained over several lattice sites (*15*).

We started with a two-dimensional (2D) ^{87}Rb Bose-Einstein condensate of a few thousand atoms confined in a single well of a standing wave, with a harmonic oscillator length of 130 nm (*16*). The condensate resided 9 μm from an in-vacuum lens that was part of an imaging system with a resolution of ~600 nm. This high-resolution system

---

[1] Department of Physics, Harvard University, Cambridge, MA 02138, USA. [2] Institut für Physik, Ludwig-Maximilians-Universität, 80799 München, Germany.

*To whom correspondence should be addressed. E-mail: greiner@physics.harvard.edu

was used to project a square lattice potential onto the pancake cloud with a periodicity of a = 680 nm, as described in (*4*). The lattice depth was ramped exponentially with a time constant of 81 ms up to a maximum depth of 16E_r, where E_r is the recoil energy of the effective lattice wavelength given by $h^2/8ma^2$ (where m is the mass of ^{87}Rb and h is Planck's constant). In a homogeneous system in two dimensions, the transition to a Mott insulator with one atom per site occurs at a ratio of interaction energy to tunneling rate of $U/J = 16.7$ (*17–19*), corresponding to a lattice depth of 12.2E_r. During this ramp, the initial transverse confinement of 9.5 Hz was increased such that the cloud size remained approximately constant. After preparing the many-body state, we imaged the atoms by increasing the lattice depth by a factor of several hundred, and then illuminated the atoms with laser cooling light that served to localize the atoms while fluorescence photons were collected by high-resolution optics. As a result of the imaging process, the many-body wave function was projected onto number states on each lattice site. In addition, light-assisted collisions immediately ejected atoms in pairs from each lattice site, leaving behind an atom on a site only if its initial occupation was odd (*20*). The remaining atoms scattered several thousand photons during the exposure time and could be detected with high fidelity. By preparing the sample repeatedly under the same conditions, we deduced the probability p_{odd} of having an odd number of atoms on a site before the measurement.

For a coherent state on a lattice site with mean atom number λ, p_{odd} is given by $\frac{1}{2}[1 - \exp(-2\lambda)] < \frac{1}{2}$. In a Mott-insulating region in the zero temperature and zero tunneling limit, $p_{\text{odd}} = 1$ for shells with an odd atom number per site, and $p_{\text{odd}} = 0$ for shells with an even atom number per site. Figure 1, A to D, shows fluorescence images in a region of the cloud as the final depth of the lattice is increased. The initial superfluid density was chosen to obtain an insulator with two shells on the Mott side of the transition; the region shown is in the outer shell containing one atom per site. For high filling fractions, the lattice sites in the images were barely resolved, but the known geometry of the lattice and imaging system point-spread function obtained from images at sparser fillings allowed reliable extraction of site occupations (*16*).

We used 24 images at each final lattice depth to determine p_{odd} for each site. The transverse confining potential varied slowly relative to the lattice spacing, and the system was, to a good approximation, locally homogeneous. We made use of this to improve the error in our determination of p_{odd} by averaging over a group of lattice sites—in this case, 51 sites for regions in the first shell and 30 sites for regions in the second shell (Fig. 1E). In the $n = 1$ shell, we detected an atom on a site with probability 94.9 ± 0.7% at a lattice depth of 16E_r. We measured the lifetime of the gas in the imaging lattice and determined that 1.75 ± 0.02% of the occupied sites were detected as unoccupied, as a result of atoms lost during the imaging exposure time (1 s) because of background gas collisions. The average occupation numbers and error bars shown in Fig. 1E include corrections for this effect.

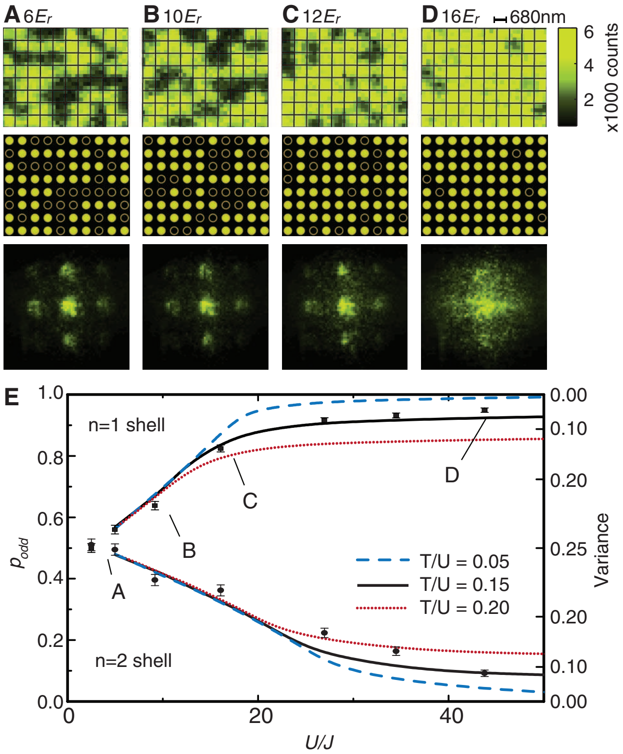

Fig. 1. Single-site imaging of atom number fluctuations across the superfluid–Mott insulator transition. (**A** to **D**) Images within each column are taken at the same final 2D lattice depth of 6E_r (A), 10E_r (B), 12E_r (C), and 16E_r (D). Top row: In situ fluorescence images from a region of 10 × 8 lattice sites within the $n = 1$ Mott shell that forms in a deep lattice. In the superfluid regime [(A) and (B)], sites can be occupied with odd or even atom numbers, which appear as full or empty sites, respectively, in the images. In the Mott insulator, occupancies other than 1 are highly suppressed (D). Middle row: results of the atom detection algorithm (*16*) for images in the top row. Solid and open circles indicate the presence and absence, respectively, of an atom on a site. Bottom row: Time-of-flight fluorescence images after 8-ms expansion of the cloud in the 2D plane as a result of nonadiabatically turning off the lattice and the transverse confinement (averaged over five shots and binned over 5 × 5 lattice sites). (**E**) Measured value of p_{odd} versus the interaction-to-tunneling ratio U/J. Data sets, with 1σ error bars, are shown for regions that form part of the $n = 1$ (squares) and $n = 2$ (circles) Mott shells in a deep lattice. The lines are based on finite-temperature Monte Carlo simulations in a homogeneous system at constant temperature-to-interaction ratio (T/U) of 0.20 (dotted red line), 0.15 (solid black line), and 0.05 (dashed blue line). The axis on the right is the corresponding odd-even variance given by $p_{\text{odd}}(1 - p_{\text{odd}})$.

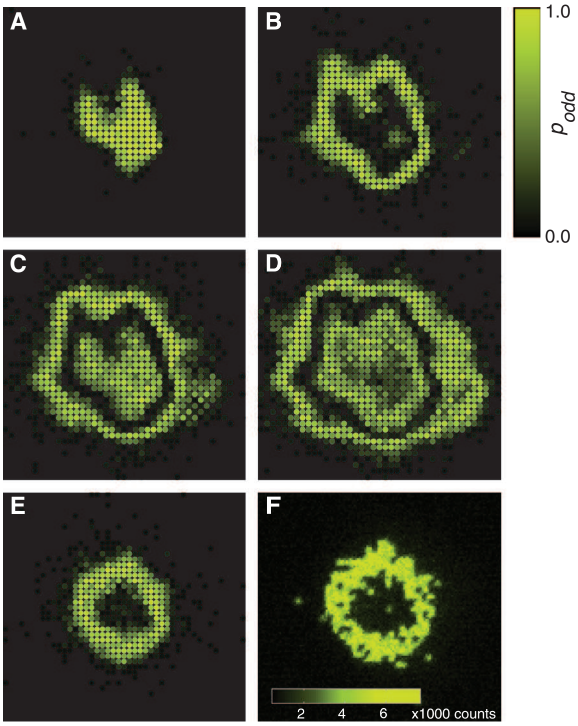

Fig. 2. Single-site imaging of the shell structure in a Mott insulator. (**A** to **D**) The images show p_{odd} on each site determined by averaging 20 analyzed fluorescence images. The lattice depth is 22E_r and the transverse confinement is 45 Hz. As the atom number is increased, the number of shells in the insulator increases from one to four. The value of p_{odd} for odd-numbered shells is close to 1; for even-numbered shells, it is close to 0. The atom numbers, determined by in situ imaging of clouds expanded in the plane, are 120 ± 10 (A), 460 ± 20 (B), 870 ± 40 (C), and 1350 ± 70 (D). (**E** and **F**) Long-wavelength disorder can be corrected by projecting an appropriate compensation light pattern onto the atoms, resulting in nearly circular shells. (E) p_{odd} (average of 20 analyzed images); (F) a single-shot raw image (arbitrary units).

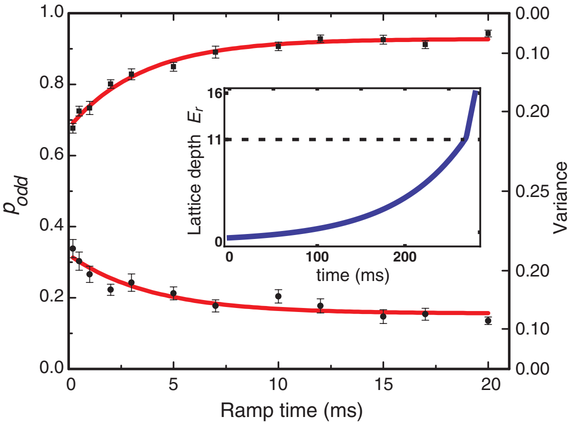

Fig. 3. Dynamics of on-site number statistics for a fast ramp from the superfluid regime to the Mott regime. p_{odd} at the end of the ramp versus ramp time is shown in the $n = 1$ (squares) and $n = 2$ (circles) shells, averaged over 19 data sets with 1σ error bars. Red lines are exponential fits. Inset shows the two-part ramp used in this experiment. The first part is a fixed adiabatic exponential ramp ($t = 81$ ms) and the second is a linear ramp starting at $11E_r$ and ending at $16E_r$. The duration of the second ramp is varied in the experiment.

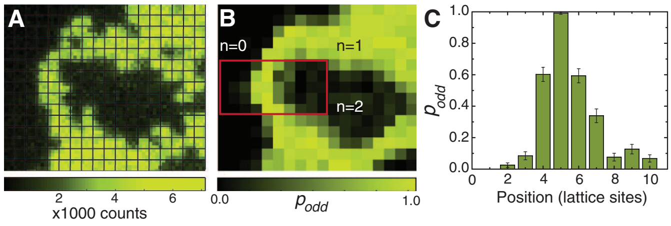

Fig. 4. Low-entropy Mott domains observed in a steep potential gradient. (**A**) Single-shot in situ image of a Mott insulator in a $16E_r$ deep lattice with 25-Hz transverse confinement. The ring is an $n = 1$ insulator enclosing an $n = 2$ region. (**B**) Average p_{odd} over 24 images. Each pixel corresponds to a single lattice site. The red rectangle encloses a region containing a Mott insulator with $n = 1$, a few lattice sites wide. (**C**) Column average of p_{odd} over the sites within the red rectangle in (B), with 1σ error bars.

Measuring the defect density in the Mott insulator provides sensitive local thermometry deep in the Mott regime. Thermometry in the Mott state has been a long-standing experimental challenge (*21*, *22*) and has acquired greater importance as experiments approach the regime of quantum magnetism (*23*–*25*), where the temperature scale should be on the order of the superexchange interaction energy. Our method directly images the excitations of the $n = 1$ Mott insulator, holes and doublons, because they both appear as missing atoms in the images. Similarly, for Mott insulators with higher fillings n, sites with excitations ($n + 1$, $n - 1$) can be detected through their opposite-parity signal. For a finite tunneling rate J much smaller than the interaction energy U, the admixture fraction of coherent hole-doublon pair excitations is $\sim(J/U)^2$, whereas any other excitations are due to incoherent thermal fluctuations and are suppressed by a Boltzmann factor, $\exp(-U/T)$.

The theory curves presented in Fig. 1E are the predicted p_{odd} in the two shells for different values of T/U. The curves were obtained using a quantum Monte Carlo "worm" algorithm (*26*, *27*), and the average temperature extracted using the data points at the three highest U/J ratios was $T/U \approx 0.16 \pm 0.03$. At the transition point for $n = 1$, this corresponds to a temperature of 1.8 nK. Assuming this value of T/U to be the overall temperature, the thin layer between the Mott shells should be superfluid, and the transition to a normal gas is expected around a critical temperature of $zJ = 2.8$ nK, where z is the number of nearest neighbors in the lattice (*28*).

Next, we studied the global structure of the Mott insulator. The high-resolution images provide an atom-by-atom picture of the concentric shell structure, including the transition layers between the insulating shells. In Fig. 2, A to D, the formation of the various shells, up to the fourth, is shown as the atom number in the trap is increased. Slowly varying optical potential disorder causes deviation from circular symmetry in the shells. The contour lines of the potential are directly seen in the images in Fig. 2. In Fig. 2, E and F, we compensated for this disorder by projecting a light pattern, generated using a digital micromirror device, through the objective (*16*), resulting in a nearly circular shell structure.

In a second series of experiments, we used on-site number statistics to probe the adiabaticity time scale for the transition, focusing on the local dynamics responsible for narrowing the number distribution. We started by increasing the lattice depth adiabatically to $11E_r$, still in the superfluid regime, using the same ramp described previously. Next, the depth was ramped linearly to $16E_r$, where, for an adiabatic ramp, a Mott insulator should form. The ramp time was varied from 0.2 to 20 ms, and p_{odd} was measured in the first and second shells as before (Fig. 3). We found that the data fit well to exponential curves that asymptotically approach the value of p_{odd} obtained in the adiabatic case. The fitted time constant in the first shell is 3.5 ± 0.5 ms; in the second shell, the constant is 3.9 ± 1.3 ms.

Relative to the critical value of the tunneling time $h/J_c = 68$ ms for the first shell, the observed dynamics were counterintuitively fast. This can be understood by using a simple picture of two atoms in a double well. In this system, as the tunneling is varied, the minimal gap between the ground state and the first excited state is U, which sets the adiabaticity time scale. It is an open question whether this argument can be generalized to a lattice. In an infinite system, the appearance of Goldstone modes in the superfluid regime leads to a vanishing gap at the transition point, but the density of states is low for energies much less than U (*29*). In fact, the $1/e$ time scale observed experimentally is comparable to $h/U_c = 4.1$ ms, where U_c is the critical interaction energy for an $n = 1$ insulator.

Although the local number statistics change on a fast time scale of h/U, entropy redistribution in the inhomogeneous potential should occur on a much slower time scale of h/J. Because superfluid and normal domains have a larger specific heat capacity than Mott domains, in an inhomogeneous system, entropy is expelled from the Mott domains and accumulates in the transition regions after crossing the phase transition if the system is in thermal equilibrium (*30*). However, in bulk Mott regions, the insulating behavior makes entropy transport difficult, and global thermalization is slow on experimental time scales (*31*). In our system, optical potential corrugations produce sizable potential gradients in some regions, leading to a heterostructure of almost 1D Mott domains, about one to two lattice sites thick, surrounded by transition layers (Fig. 4). We found remarkably low defect densities and sharp transitions between superfluid and Mott states in these regions. The measured defect probability per site in the domain shown is 0.8 ± 0.8%. In these microscopic domains, each site of a Mott domain is in contact with a superfluid region. Such a configuration is likely to lead to fast thermalization, which would explain the low defect density we observed. This suggests that the lowest entropies in a Mott insulator might be obtained under conditions where the chemical potential is engineered so as to obtain alternating stripes (2D) or layers (3D) of insulating and superfluid regions (*32*, *19*).

In addition to the number statistics studied in this work, single-site imaging could be applied to study spatial correlations in strongly correlated quantum gases (*33*), and to directly measure entanglement in a quantum information context. The low-defect Mott states we detect would provide an ideal starting point for quantum magnetism experiments; if the low entropy in the Mott domains can be carried over to spin models, it should be possible to realize magnetically ordered states such as antiferromagnets, which could be directly detected with single-site imaging.

References and Notes

1. K. M. Lang *et al.*, *Nature* **415**, 412 (2002).
2. T. Basché, W. E. Moerner, M. Orrit, U. P. Wild, *Single-Molecule Optical Detection, Imaging and Spectroscopy* (Wiley-VCH, Cambridge, 1997).
3. X. Zhuang *et al.*, *Science* **288**, 2048 (2000).

4. W. S. Bakr, J. I. Gillen, A. Peng, S. Fölling, M. Greiner, *Nature* **462**, 74 (2009).
5. M. P. A. Fisher, P. B. Weichman, G. Grinstein, D. S. Fisher, *Phys. Rev. B* **40**, 546 (1989).
6. D. Jaksch, C. Bruder, J. I. Cirac, C. W. Gardiner, P. Zoller, *Phys. Rev. Lett.* **81**, 3108 (1998).
7. M. Greiner, O. Mandel, T. Esslinger, T. W. Hänsch, I. Bloch, *Nature* **415**, 39 (2002).
8. R. Jördens, N. Strohmaier, K. Günter, H. Moritz, T. Esslinger, *Nature* **455**, 204 (2008).
9. U. Schneider *et al.*, *Science* **322**, 1520 (2008).
10. B. Capogrosso-Sansone, E. Kozik, N. Prokof'ev, B. Svistunov, *Phys. Rev. A* **75**, 013619 (2007).
11. M. Greiner, O. Mandel, T. W. Hänsch, I. Bloch, *Nature* **419**, 51 (2002).
12. F. Gerbier, S. Fölling, A. Widera, O. Mandel, I. Bloch, *Phys. Rev. Lett.* **96**, 090401 (2006).
13. S. Fölling, A. Widera, T. Müller, F. Gerbier, I. Bloch, *Phys. Rev. Lett.* **97**, 060403 (2006).
14. G. K. Campbell *et al.*, *Science* **313**, 649 (2006).
15. N. Gemelke, X. Zhang, C. L. Hung, C. Chin, *Nature* **460**, 995 (2009).
16. See supporting material on *Science* Online.
17. M. Köhl, H. Moritz, T. Stöferle, C. Schori, T. Esslinger, *J. Low Temp. Phys.* **138**, 635 (2005).
18. I. B. Spielman, W. D. Phillips, J. V. Porto, *Phys. Rev. Lett.* **98**, 080404 (2007).
19. B. Capogrosso-Sansone, Ş. Söyler, N. Prokof'ev, B. Svistunov, *Phys. Rev. A* **77**, 015602 (2008).
20. M. T. DePue, C. McCormick, S. L. Winoto, S. Oliver, D. S. Weiss, *Phys. Rev. Lett.* **82**, 2262 (1999).
21. D. M. Weld *et al.*, *Phys. Rev. Lett.* **103**, 245301 (2009).
22. S. Trotzky *et al.*, http://arxiv.org/abs/0905.4882 (2009).
23. L. M. Duan, E. Demler, M. D. Lukin, *Phys. Rev. Lett.* **91**, 090402 (2003).
24. E. Altman, W. Hofstetter, E. Demler, M. D. Lukin, *N. J. Phys.* **5**, 113 (2003).
25. S. Trotzky *et al.*, *Science* **319**, 295 (2008).
26. N. V. Prokof'ev, B. V. Svistunov, I. S. Tupitsyn, *Phys. Lett. A* **238**, 253 (1998).
27. L. Pollet, K. V. Houcke, S. M. Rombouts, *J. Comput. Phys.* **225**, 2249 (2007).
28. F. Gerbier, *Phys. Rev. Lett.* **99**, 120405 (2007).
29. M. Knap, E. Arrigoni, W. von der Linden, *Phys. Rev. B* **81**, 024301 (2010).
30. L. Pollet, C. Kollath, K. Van Houcke, M. Troyer, *N. J. Phys.* **10**, 065001 (2008).
31. C. L. Hung, X. Zhang, N. Gemelke, C. Chin, *Phys. Rev. Lett.* **104**, 160403 (2010).
32. M. Popp, J. Garcia-Ripoll, K. G. Vollbrecht, J. I. Cirac, *Phys. Rev. A* **74**, 013622 (2006).
33. E. Kapit, E. Mueller, http://arxiv.org/abs/1004.4903 (2010).

34. We thank G. Jotzu, E. Demler, D. Pekker, B. Wunsch, T. Kitagawa, E. Manousakis, W. Ketterle, and M. D. Lukin for stimulating discussions. Supported by a grant from the Army Research Office with funding from the Defense Advanced Research Projects Agency Optical Lattice Emulator program, and grants from Air Force Office of Scientific Research Multidisciplinary University Research Initiative, NSF, an Alfred P. Sloan Fellowship (M.G.), and the Swiss National Science Foundation. The simulations were run on the Brutus cluster at ETH Zürich.

Supporting Online Material

www.sciencemag.org/cgi/content/full/science.1192368/DC1
Materials and Methods
References

17 May 2010; accepted 8 June 2010
Published online 17 June 2010;
10.1126/science.1192368
Include this information when citing this paper.

Ultrathin PbS Sheets by Two-Dimensional Oriented Attachment

Constanze Schliehe,[1] Beatriz H. Juarez,[2] Marie Pelletier,[1] Sebastian Jander,[1] Denis Greshnykh,[1] Mona Nagel,[1] Andreas Meyer,[1] Stephan Foerster,[1] Andreas Kornowski,[1] Christian Klinke,[1] Horst Weller[1]*

Controlling anisotropy is a key concept in the generation of complex functionality in advanced materials. For this concept, oriented attachment of nanocrystal building blocks, a self-assembly of particles into larger single-crystalline objects, is one of the most promising approaches in nanotechnology. We report here the two-dimensional oriented attachment of lead sulfide (PbS) nanocrystals into ultrathin single-crystal sheets with dimensions on the micrometer scale. We found that this process is initiated by cosolvents, which alter nucleation and growth rates during the primary nanocrystal formation, and is finally driven by dense packing of oleic acid ligands on {100} facets of PbS. The obtained nanosheets can be readily integrated in a photodetector device without further treatment.

Controlled assembly leading to anisotropic nanostructures poses a conceptual challenge in the field of materials research. Penn and Banfield *et al.* (*1*, *2*) described crystal growth, in which oxide nanoparticles coalesce in well-defined crystalline orientations. Their method of oriented attachment of nanocrystals is now one of the most favorable techniques to grow linear or zig-zag–type one-dimensional (1D) nanostructures. In addition to strong size-quantization effects occurring in these structures, their big advantage is solution processability, which makes them attractive candidates for optoelectronic and thermoelectric applications in low-cost integrated systems. 1D assemblies of oriented attachment have been reported, and, in most cases, the anisotropy during self-assembly is caused by crystal planes with preferred reactivity and dipole moments in the crystallites. However, systems with cubic-crystal symmetry (such as PbS and PbSe), in which beautiful 1D oriented attachment occurs, are somewhat more difficult to explain. Oriented attachment, in this case, should result in 3D networks rather than 1D structures. The common explanation assumes that, despite the strict monodispersity of the samples, inhomogeneities in the chemical composition of surface planes exist and result in dipole moments within the nanocrystals. On the other hand, organic ligand molecules play a crucial role in such processes by capping nanoparticle surfaces selectively and may hinder, modify, or trigger an oriented attachment (*3*). In this work, we show that the formation of ordered and densely packed ligand surface layers of oleic acid on {100} PbS surfaces can drive the normally isotropic crystal growths into a 2D oriented attachment of nanocrystals. In addition, the presence of chlorine-containing cosolvents during the initial nucleation and growth process of the nanocrystals plays a prominent role.

Syntheses of lead chalcogenide nanoparticles (*4*–*7*) can lead to a large variety of particle shapes through slight changes of the reaction conditions. The mechanism of how small traces of organophosphine compounds may alter the course of the reactions has been reported, which underlines their complexity (*8*). For other systems, like CdS nanoparticles, shape control has been reported by the addition of small amounts of HCl (*9*) or chlorine-containing solvents such as 1,2-dichloroethane (DCE); for example, in the case of CdSe nanorods attached to carbon nanotubes (*10*). Reported strategies to generate 2D nanostructures are based on the use of lamellar-like templates (*11*) or thin superstructures by assembly (*12*–*14*).

Our approach is based on a standard synthetic procedure to generate nearly spherical PbS nanoparticles (*15*). After 3 min, the resulting dotlike particles have a mean diameter of ~5 nm. In contrast, ultrathin PbS nanosheets, as depicted in Fig. 1, are formed in the presence of chlorine-containing compounds such as DCE or similar linear chloroalkanes (fig. S1). The nanosheets have lateral dimensions of several hundred nanometers and stack showing Moiré patterns caused by the interference between the crystalline lattices of the individual sheets (see fig. S2 for Moiré patterns and corresponding simulations).

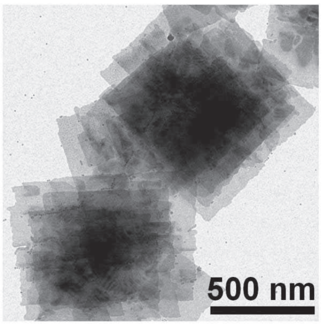

Fig. 1. TEM image of stacked PbS nanosheets using 1,1,2-trichloroethane.

---

[1] Institute of Physical Chemistry, University of Hamburg, 20146 Hamburg, Germany. [2] IMDEA Nanoscience, Ciudad Universitaria de Cantoblanco 28049, Madrid, Spain.

*To whom correspondence should be addressed. E-mail: weller@chemie.uni-hamburg.de